Taylor & Francis
Taylor & Francis Group

Heterolayered carbon allotrope architectonics *via* multi-material 3D printing for advanced electrochemical devices

Mario Palacios-Corella[a], Michela Sanna[a], José Muñoz[a], Kalyan Ghosh[a], Stefan Wert[a] and Martin Pumera[a,b,c]

[a]Future Energy and Innovation Laboratory, Central European Institute of Technology, Brno University of Technology, Brno, Czech Republic; [b]Faculty of Electrical Engineering and Computer Science, VSB – Technical University of Ostrava, Ostrava, Czech Republic; [c]Department of Medical Research, China Medical University Hospital, China Medical University, Taichung, Taiwan

ABSTRACT

3D printing has become a powerful technique in electrochemistry for fabricating electrodes, thanks to readily available conductive nanocomposite filaments, such as those based on carbon fillers (i.e., carbon nanotubes (CNTs) or carbon black (CB)) within an insulating polymeric matrix like polylactic acid (PLA). Inspired by inorganic heterostructures that enhance the functional characteristics of nanomaterials, we fabricated hetero-layered 3D printed devices based on carbon allotropes using a layer-by-layer assembly approach. The heterolayers were customised through the alternate integration of different carbon allotrope filaments via a multi-material 3D printing technique, allowing for a time-effective method to enhance electrochemical performance. As a first demonstration of applicability, CNT/PLA and CB/PLA filaments were utilised to construct ordered hetero-layered carbon-based electrodes. This contrasts with conventional methods where various carbon species are mixed in the same composite-based filament used for building electrochemical devices. Multi-material 3D-printed carbon electrodes exhibit improved electrochemical performance in energy conversion (e.g., hydrogen evolution reaction or HER) and sensing applications (e.g., ascorbic acid detection) compared to single-material electrodes. This work paves the way for manufacturing advanced 3D-printed heterolayered electrodes with enhanced electrochemical activity through multi-material 3D printing technology.

1. Introduction

3D printing (also termed additive manufacturing) is probably one of the most revolutionary technologies developed during the twentieth century [1]. By following a bottom-up approach, 3D printing has gathered increasing interest in recent years as it allows for the fast production of structures by taking advantage of a layer-by-layer deposition of the desired material. The increasing amount of users has facilitated its fast development and implementation in many manufacturing processes [2]. Complex geometries, a very low amount of waste, and cost-effective production of structuralised materials are the principal benefits [3] of this technique that hasn't gone unnoticed by the scientific community. In this line, during the last decade, 3D printing has been exploited in the fabrication of structures employed in a wealth of scientific fields [4] and applications, such as (bio)sensing [5–14], (electro)catalysis [15–20], or micro-robotics [21–24]. The high applicability of 3D printing has also reached the attention of the electrochemistry community due to its potential applicability for the printing of 3D electrodes [25], preparation of logic gates [26], processors [27], or devising of electrochemical energy storage devices [28–32]. Particularly, for electronics manufacturing, fused deposition modelling (FDM) is one of the most appealing 3D printing methods because of its versatility and fast preparation of products [33]. In FDM, polymer-based filaments are molten in a movable nozzle to create the individual layers that compose the final object. Within the extensive library of polymers employed to prepare filaments, polylactic acid (PLA), acrylonitrile butadiene styrene (ABS), or Nylon could be highlighted as the most recurrent. However, the insulating nature of these polymers hinders their direct use for electronic applications.

To increase their conductivity, filaments consisting of mixtures of carbon allotropes embedded in a polymer matrix have been developed and commercialised, such as graphite/ABS [34,35], carbon nanotubes (CNTs)/PLA [36,37], or carbon black (CB)/PLA [38–40], which in turn have paved the way for the advance in the electrochemistry field through the preparation of 3D-printed carbon electrodes (3D-PCEs) [40,41].

Carbon nanomaterials have emerged as strong candidates for electrochemical sensing due to their extraordinary properties on the nanoscale [42,43]. On the one hand, the diversity of chemical bonds displayed by carbon atoms, which can range from sp^3 to sp^1 hybridised states, give rise to different allotropic forms (e.g. CNTs, carbon fibres, fullerenes, etc.) that show distinct physicochemical properties and, additionally, exhibit different electrochemical surface area, conductivity or structure hybridisation [44]. However, besides these very interesting characteristics, carbon materials present intrinsic constraints that the materials science community has been minimising by merging them in harmoniously built heterostructures that consist of a layer-by-layer assembly of different 2D materials such as graphene/h-BN [45] or MoS_2/graphene [46]. The final heterostructures exhibit remarkable properties due to the synergistic effect of the parent single layers. These important results motivate even more the development of heterolayered 3D printed structures that could combine several functionalities. Indeed, since the first 3D printed structure was built, the technique has advanced considerably within the electrochemistry community, which has enabled the preparation of carbon composite filaments or inks [47] that can be further chemically modified [48], leading to improved or tunable properties of the final carbon electrode [49,50]. In addition, a combination of functionalities could easily be achieved in the future by integrating materials with very different properties. However, the development of heterostructures by 3D printing is nowadays an unmatured field.

Thus, 3D printing, through Multi-material 3D printing, can enable the precise engineering of heterolayers *via* a print-pause-print approach in which a second functional material can be integrated with the first material by temporal disruption of the printing process in a time-effective robotic controlled manner [51]. The multi-material 3D printing approach could be considered the FDM alternative to the electrochemical double nozzle approach [52,53], and reveals itself as a strong candidate for combining different carbon allotropes since it allows for combining different filaments at the user's demand contrasting with conventional 3D printing, where only one filament can be used for the printing of a single structure. Mechanically, in multi-material 3D printing, a robotic body with a rotating pulley barrel and a single extruder motor pull up different filaments when they must be loaded, allowing for a fast and fully automatised process. Thus, multi-material 3D printing would be a potential strategy to combine different carbon allotropes in 3D-PCEs *via* the formation of heterolayers. Importantly, the exploration of such heterolayered materials as 3D printed devices for electrochemical applications such as energy conversion (hydrogen evolution reaction, HER) or sensing of chemical species is an unexplored field and their study could pave the way towards more efficient sensors or energy devices.

Herein, the prototype of a heterolayered multi-material 3D-printed carbon electrode (MM 3D-PCE) has been devised *via* multi-material 3D printing technology by alternating the deposition of two different commercially available carbon filaments (i.e. PLA/CNT and PLA/CB). In the first section of the work, morphological and structural characterisation performed on all the electrodes show that an asymmetry is achieved in the MM 3D-PCE, exposing both carbon allotropes on the different surfaces of the electrode, contrary to that observed in the pure material electrodes. Electrochemical characterisation of the electrodes using cyclic voltammetry performed on a conventional ferrocenemethanol (FcMeOH) redox marker reveals that MM 3D-PCEs present hybrid features between those of 3D-PCEs purely based on CNT or CB filaments, giving rise to calculated electrochemical parameters between those of the pure materials, although statistical analysis reveals no significant differences between electrodes. In the second and third sections of the work, it is demonstrated that this intermediate behaviour turns into a superior electroactivity when the hydrogen evolution reaction (HER) is investigated, as the MM 3D-PCEs show an improved performance of around 40% compared to the closest pure material electrode. Similarly, when the detection of ascorbic acid (AA) is the object of study, the MM 3D-PCEs show improved response giving rise to a sensibility 1.2 times better than that of the pure material electrodes. Thus, this work offers a novel strategy for the development of MM 3D-PCEs *via* multi-material 3D printing for the preparation of advanced 3D-PCEs exhibiting improved electrochemical performances for task-specific applications.

2. Experimental

2.1. Materials and chemicals

The CB/PLA and CNT/PLA (brand name 'Black Magic') filaments used herein were commercially available and

purchased from Proto-Pasta, USA, and Graphene Laboratories Inc., USA, respectively. N,N-Dimethylformamide (DMF) used for the chemical activation of printed electrodes was purchased from Sigma-Aldrich, Germany. The electrochemical activity of the electrodes was studied in a 1.5 mM aqueous solution of ferrocenemethanol (FcMeOH, 99%, ABCR GmbH, Germany) and 0.2 M in potassium nitrate (KNO_3, analytical grade, Merck KGaA, Germany). For studying their activity for the HER, 0.5 M sulfuric acid (H_2SO_4, 96%, analytical grade, Penta, Czech Republic) was used. Deionised water with a resistivity >18.2 MΩ cm (Milli-Q Advantage A10 system, Germany) was used to prepare solutions. Ascorbic acid was purchased from Merck and used without further purification.

2.2. Apparatus and software

Modelling of the 3D-PCE was done using Autodesk Fusion 360 software. The slicing of the designed models was done using the PrusaSlicer 2.4.0 software. The electrodes were printed using a Prusa i3 MK3s printer which was upgraded with an MMU2s multi-material unit (Prusa Research, Czech Republic). A ruby-tipped 0.6 mm diameter nozzle (Olsson, 3DVerkstan, Sweden) was used for filament extrusion. The electrodes' morphology was assessed by scanning electron microscopy (SEM) using a LYRA 3 SEM (Tescan, Czech

Republic). The surface composition of the materials was analysed by high-resolution X-ray photoelectron spectroscopy (XPS) using a Kratos (Axis Supra, UK), and Raman spectroscopy using an Alpha 300R (Witec, Oxford). Structural information was acquired by powder X-ray diffraction (PXRD) using a Rigaku Smartlab 3 kW (Rigaku, Japan). Electrochemical studies were carried out using a potentiostat (PGSTAT 204, Autolab, Netherlands). A Pt rod and an Ag/AgCl (saturated KCl) were used as counter and reference electrodes.

2.3. Electrode preparation

MM 3D-PCEs were printed *via* multi-material 3D printing technology and had a lollipop-like shape consisting of 4 alternating horizontal layers of CNT/CB materials as shown in Figure 1(B). The base layer was printed with CNT filament, while the second layer was printed with CB filament, and so on with the filament being automatically changed after each layer deposition to integrate CNT/CB heterolayers. Specifically, each layer was set to a thickness of 0.15 mm. The circular head of the electrodes had a radius of 3 mm (6mm diameter), and the electrode rod had a width of 3.5 and 15 mm in length. For all the electrodes in this work, a 0.6 mm nozzle heated to 220°C was employed to melt the filaments. The infill pattern was set to 15%, and the bed printing temperature was fixed to 60°C to ensure the best adhesion of
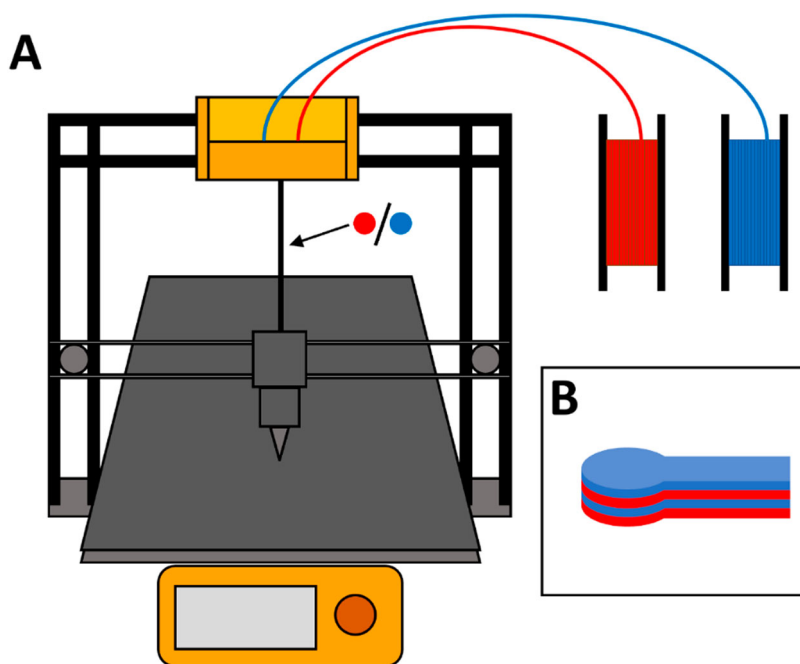

Figure 1. (A) Schematic representation of the multi-material 3D printer setup used to fabricate the heterolayered electrode by combining CNT (blue) and CB (red) filaments. (B) Schematic structure of the printed multi-material electrode with a total of four layers. Dimensions are not for scale.

the printed filament. For reference purposes, single material 3D-PCEs were printed solely using either CNT/PLA or CB/PLA filaments. All the electrodes used throughout the work were printed using the aforementioned parameters. Activation of 3D-PCEs was performed by wet-chemical activation in DMF for 1 h to partially remove the PLA and increase their conductivity [54]. In short, glass vials were filled with DMF, and the 3D-PCEs electrodes were introduced individually in each vial in a standing position. After one hour immersed in the DMF, the solvent was removed, and the electrodes were successively washed three times with abundant water and three times with ethanol followed by an overnight drying process under the air.

2.4. Electrochemical measurements

For electrochemical characterisation of the electrodes, cyclic voltammograms were recorded using a 1.5 mM FcMeOH redox marker solution containing 0.5 M KNO_3 as a supporting electrolyte. CVs were run three times between −0.4 and 1 V at a scan rate of 50 mV s^{-1}. For investigating the electrodes' activity towards the hydrogen evolution reaction (HER), linear sweep voltammograms (LSVs) were recorded in a 1 M H_2SO_4 aqueous solution. A linearly decreasing potential ranging from 0.0 V to −1.4 V was applied to the 3D-printed electrodes, with a scan rate of 5 mV s^{-1}. For sensing approaches, ascorbic acid (AA) was used as a model analyte. Different concentrations of analyte (2.5, 5, 10, 25, 50, 100, and 200 μM) were recorded by differential pulse voltammetry (DPV) using a 0.1 M HNO_3/KNO_3 electrolyte solution (scan rate: 50 mV s^{-1}).

2.5. Statistical analysis

Unless otherwise stated, every electrochemical experiment was carried out three times for each type of electrode. For the calculation of electrochemical parameters and statistical values, the average of the three electrodes was calculated with the corresponding standard deviation expressed as the error of the value. For the data contained in Table 1, one-way ANOVA statistical analyses were carried out using Origin Pro software. For all the analyses carried out, the significance level was set to 0.05.

3. Results and discussion

The materials characterisation of multi-material 3D-printed electrodes was carried out after their fabrication and activation with DMF for 1 h, which allowed to partially remove the PLA from the surface of the printed structures. The morphology of the electrodes was analyzed using SEM (Figure 2). Both reference carbon electrodes (CNT and CB 3D-PCEs) showed their characteristic morphology observed previously after chemical activation [40,41,55]. Entangled carbon nanotubes (1D) (Figure 2(A)) for CNT 3D-PCEs or aggregates of very small nanosphere-shaped carbon particles (3D) (Figure 2(B)) for CB 3D-PCEs are observed and allow to distinguish between both materials easily under the electronic microscope. To better understand the hetero-layered structure of the MM 3D-PCEs, two different SEM images were captured (Figure 2(C–D)), one from the bottom side and one from the top side, as the asymmetric nature of the electrode should render two sides with a very distinct morphology. SEM images of the bottom side of MM 3D-PCE reveal the typical morphology of CNT 3D-PCEs (Figure 2(C)) again. On the other hand, the pictures obtained for the top side (Figure 2(D)) stand out as it combines the presence of both carbon allotropes on the surface, similar to that observed in the 3D-printed electrodes from the commercial hybrid CNT/CB filament [50]. The presence of these CNTs on the top side of the MM-3DPCEs could be explained by the activation procedure with DMF. Upon removal of the outer layers of PLA of the electrode's surface, CNTs are released from the bottom side of the MM-3DPCEs and stay in suspension in the DMF until the solvent is removed, when some of the CNTs transfer and deposit onto the top side of the electrode.

After assessing the morphology of the 3D-PCEs, the physicochemical properties of the different electrodes were studied by XPS, RAMAN spectroscopy, and PXRD, which allowed the differentiation of structural characteristics of the carbon allotropes. XPS was used to analyze the different contributions resulting from the carbon allotropes. In the XPS measurements, the sample is irradiated with X-rays, which leads to the photoemission of electrons with a given kinetic energy recorded in a detector. It should be noted that every element of the periodic table photoemits electrons with characteristic kinetic energy, allowing their identification in the

Table 1. Principal electrochemical parameters calculated from CV data (average values from 3 electrodes).

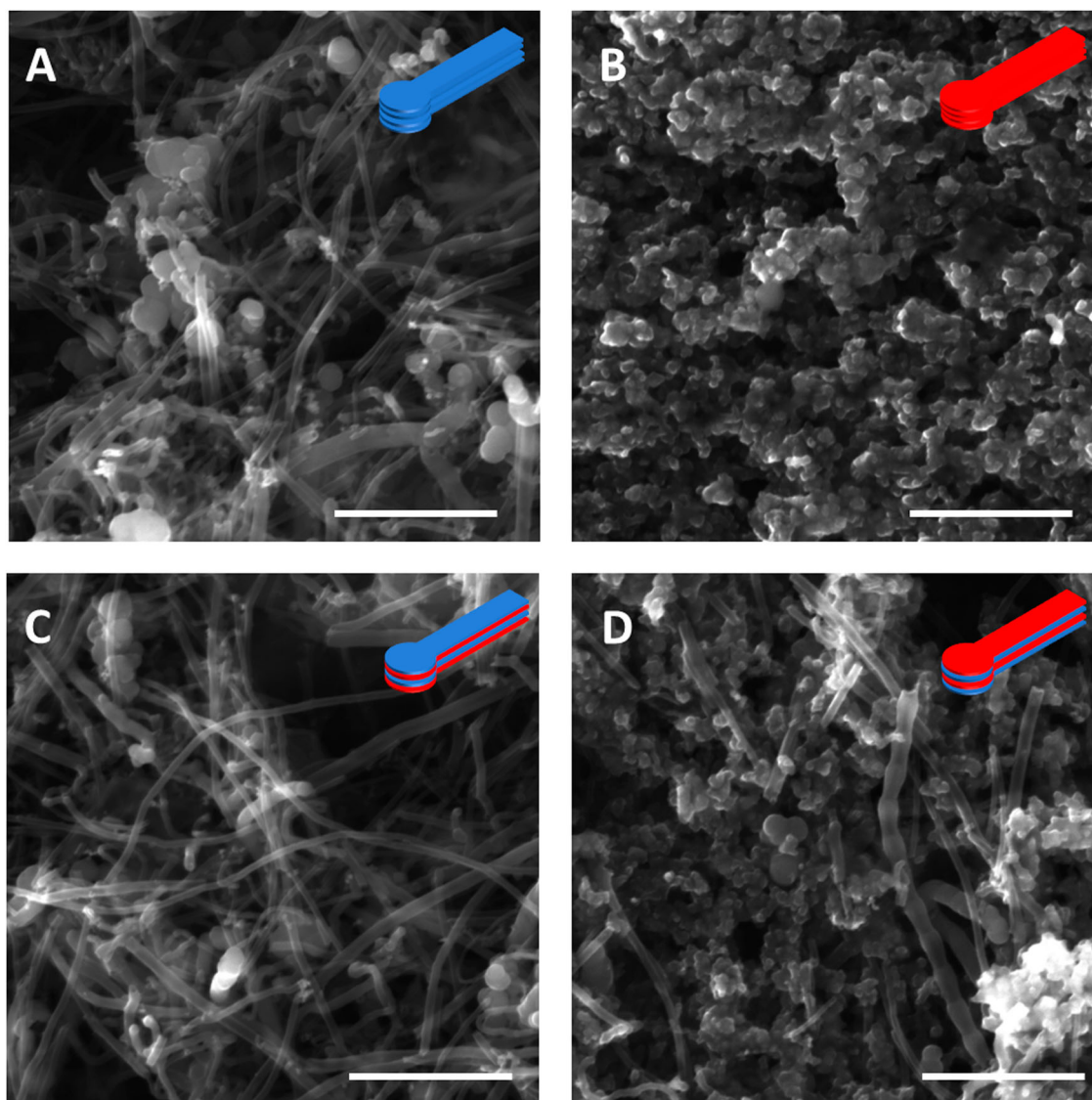| 3D-PCE	I_{pa}/I_{pc}	i_0 (μA)	ΔEp (mV)	k^0 (cm·s^{-1})	A (cm^2)	R_{ct} (kΩ)
MM	0.91 (±0.03)	23.5 (±0.5)	258 (±29)	3.95×10^{-4} (±1.7×10^{-4})	0.40 (±0.03)	1.10 (±0.03)
CNT	0.94 (±0.02)	25.1 (±0.5)	320 (±35)	1.7×10^{-4} (±0.9×10^{-4})	0.43 (±0.04)	1.02 (±0.02)
CB	0.88 (±0.03)	19.5 (±0.9)	204 (±10)	7.77×10^{-4} (±0.9×10^{-4})	0.45 (±0.03)	1.32 (±0.06)

Figure 2. SEM images of DMF-activated CNT 3D-PCE (A), CB 3D-PCE (B), MM 3D-PCE bottom side (C), MM 3D-PCE top side (D). Scale bars: 2 μm.

sample. Thus, the C 1s core level signal detected for CNT and CB 3D-PCEs was deconvoluted into different components that have been assigned to C 1s (sp^2), C 1s (sp^3), C 1s (C–O), C 1s (C=O), and C 1s (O=C–O) from lower to higher binding energy and are in good agreement with previous findings for these 3D-PCEs (Figure 3(A–B)) [55]. The latter three and the sp^3 components are usually associated with the PLA matrix, while the sp^2 component corresponds to the C=C bonds present in the graphitic carbon [41,56]. In addition, the presence of C=O and C–O groups can also be associated with the oxidised form of graphitic carbon, especially in the case of the carbon black filament, and this oxidation has been demonstrated to have important effects in the roughness and different electrochemical parameters [57–59]. Furthermore, the significant C–O

peak in the C1s spectrum of CB 3D-PCEs (shown in Figure 3(B)) suggests the presence of a substantial amount of PLA that was not eliminated during DMF activation [60]. Thus, the bottom side of the MM-3DPCEs gave rise to very similar C 1s contributions to those observed for CNT 3D-PCEs, as expected, due to their similar composition. When compared with the pure CB 3D-PCE, the top side of the MM 3D-PCE showed a decreased contribution from C 1s (C–O) and C 1s (C= O) with respect to the C 1s (sp^2) and C 1s (sp^3) peaks, whose origin is associated with the deposition of CNTs on the top side of the electrode (Figures 3(C–D)). XPS was additionally employed to evaluate the presence of metal impurities in all the electrodes. Metallic impurities are common metallic contamination is common in CNT filaments, and the origin of the metals can be found in
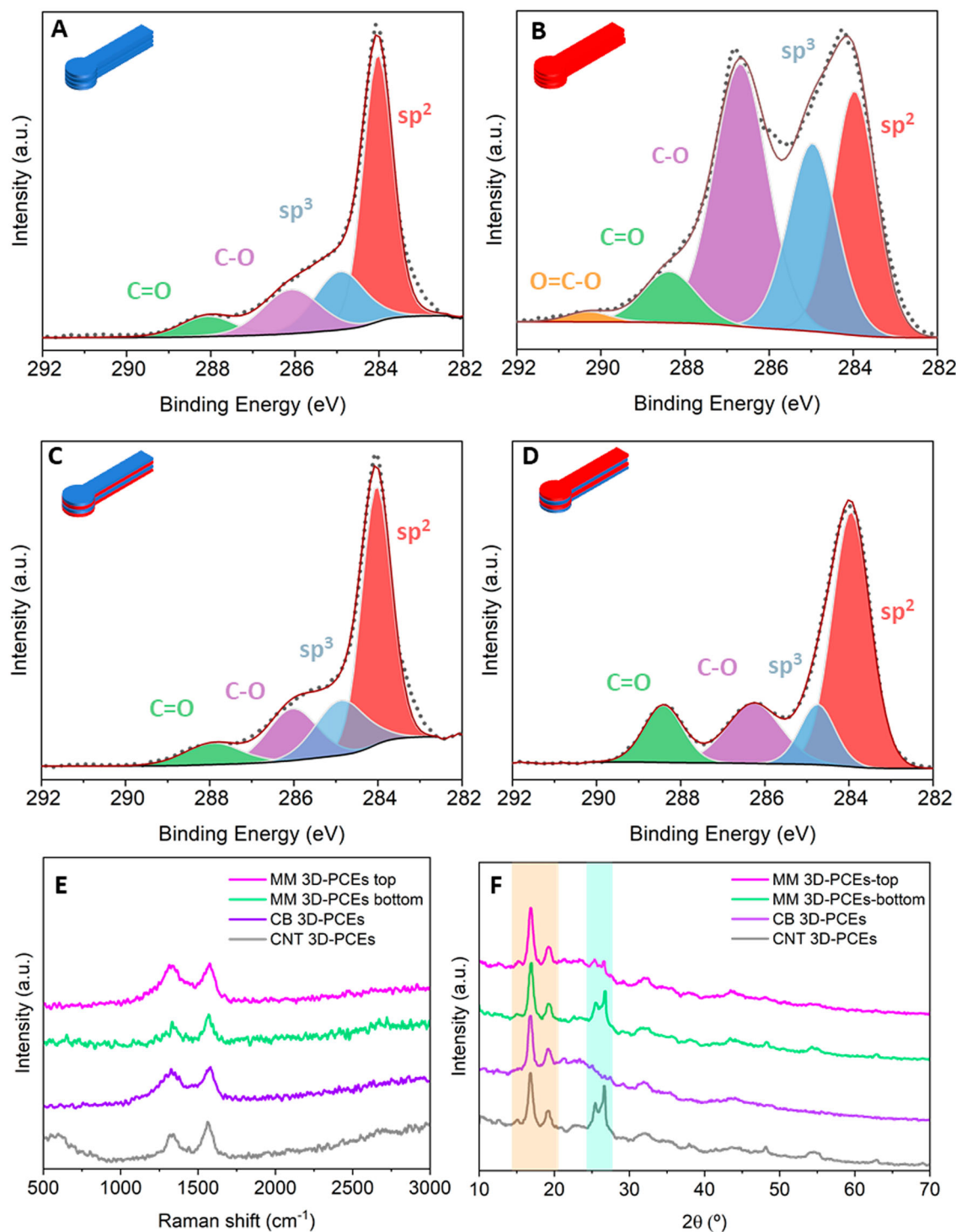
Figure 3. XPS analysis of CNT 3D-PCE. (A) CB 3D-PCE. (B) MM 3D-PCE bottom side. (C) MM 3D-PCE top side; PXRD of all the electrodes. (E) and Raman spectroscopy of all the electrodes (F).

the experimental preparation of the nanotubes [17,61]. On the other hand CB filaments have not been widely studied and the presence of impurities is uncertain. Thus, wide spectra were collected for all the electrodes (Figure S1) corroborating the presence of Ti (0.2% at.) and Fe (0.06% at.) impurities on CNT 3D-PCEs and the

bottom side of MM 3D-PCEs. Contrarily, metal impurities were not detected either on CB 3D-PCEs or the top side of MM 3D-PCEs. To get more insight into the nature of the carbon present in all the electrodes, Raman spectroscopy was employed as an important technique. In the Raman technique, the sample is irradiated with

light of a fixed monochromatic wavelength. Following, the interaction of the light with the bonds of the chemical species present in the sample provokes a shift of the monochromatic light towards higher or lower wavenumbers through scattering and is registered in the detector. The Raman scattering allows the assessment of the D and G bands ratio, which is commonly used as a metric to characterise the density of defects in the carbon allotropes [62]. In this regard, both bands were found in the Raman spectra acquired for pure material CNT and CB 3D-PCEs around 1300 and 1600 cm^{-1}, respectively. The spectra for both electrodes show marked differences between them with calculated I_D/I_G band ratios of 0.69 and 0.94, respectively (Figure 3(E)), allowing us to conclude that there is a higher degree of disorder in the carbon particles found in CB 3D-PCEs compared to the nanotubes that comprise CNTs-based electrodes [63]. The spectrum collected for the bottom side of MM 3D-PCEs reveals, again, an important similarity to that recorded for CNT 3D-PCEs, with a calculated I_D/I_G band ratio of 0.73. As expected, the same spectrum measured for the top side of MM 3D-PCEs gives rise to a calculated I_D/I_G band ratio of 0.95, corroborating the strong presence of highly disordered CB black particles.

To conclude the physicochemical characterisation, PXRD was used as a powerful technique to analyse the structure of the carbon species present on the surface of the carbon electrodes. In this technique, X-rays are focused on the sample with the constant movement of the generator and or detector theta angles with respect to the sample, and the diffracted X-rays by the sample are collected in the detector, allowing to obtain diffraction patterns characteristic of each sample, which further allow obtaining atomic and plane positions. Scans run for all 3D-PCEs (Figure 3(F)) showed two main peaks at 2θ of 17 and 19.3° which, according to previous reports, arise from the crystalline PLA polymer present in the electrode [64]. When CNT and CB 3D-PCEs diffraction patterns are compared at higher 2θ values, two important diffraction peaks can be found at 2θ 25.3 and 26.7° for CNT 3D-PCEs, but not for CB 3D-PCEs. These peaks correspond to the interlayer spacing between layers of CNTs and are closely related to the diameter of the CNTs, which further corroborates the high dispersity of CNTs in our electrodes [65,66]. The bottom side of the MM 3D-PCEs inherits the diffraction pattern observed for CNT 3D-PCEs, whilst the top side diffraction pattern shares an important similarity with the diffraction pattern observed for CB 3D-PCEs with the additional contribution of the CNTs deposited on the top layer during the activation procedure (see above). Finally, the surface conductivity of all the electrodes was determined by using a conventional 2-probe system. By measuring the surface resistance between two points separated by 1 cm in 4 different electrodes of each type, we obtained the conductivity of the surface of the 3D-PCEs. Thus, CNT and CB 3D-PCEs show conductivities of 44.0 ± 0.4 and 86.8 ± 0.8 mS/m, respectively. MM 3D-PCEs' bottom and top sides had 35.8 ± 0.3 and 86.6 ± 3.1 S/m, respectively. These results further confirm the asymmetric conductivity of the electrodes MM 3D-PCEs, which matches the physicochemical properties characterised above.

After assessing the physicochemical characteristics of the 3D-PCEs, their electrochemical properties were evaluated. We focused on three important reactions: outer sphere heterogeneous electron transfer rate (using ferrocene methanol, FcMeOH), adsorption/desorption-driven hydrogen evolution, and oxidation of an important biomolecule. We first studied the heterogeneous electron transfer rate using cyclic voltammetry. Before getting into the analysis of the electrochemical data, it should be pointed out that the different filaments employed in this work present different carbon contents (e.g. CNT filament is advertised by the manufacturer to contain less than 20% carbon, while CB filament is 21.4%). To avoid any misleading conclusion as a consequence of the difference in carbon content and to add cost-efficiency dimensionality, the CV data presented below has also been normalised per gram of carbon and can be found in the supporting information (Figures S2 and S3 and Table S1). In addition, the prototypical $Fe(CN)_6^{4-}$/$Fe(CN)_6^{3-}$ redox marker was also tested (Figure S4), delivering suboptimum results, as has been observed in these 3D-printed carbon electrodes previously [67,68]. Unless otherwise stated, the data presented for MM 3D-PCEs always corresponds to the electrode with both faces exposed to the electrolyte.

Cyclic voltammograms of all the 3D-PCEs (Figure 4(A–C)) show well-defined oxidation and reduction peaks for the FcMeOH redox marker. In terms of width, CNT 3D-PCEs show wider oxidation and reduction peaks, while both MM and CB 3D-PCEs presented narrower peaks. Table 1 shows the most relevant parameters calculated from CV data for the different 3D-PCEs (information on the calculations can be found on the SI). The calculated anodic-to-cathodic peak current ratios (I_{pa}/I_{pc}) remain below 1 in all cases. In addition, these peak current ratios make it clear that the reversibility of oxidation or reduction reactions is higher on the surface of the CNT 3D-PCEs followed closely by MM 3D-PCEs and finally by CB 3D-PCEs. In this line, the highest exchange current intensity, i_0, calculated by the Tafel extrapolation of scans registered at 5 mV s^{-1} (Figure S5), is also displayed by the CNT 3D-PCEs followed by MM and CB
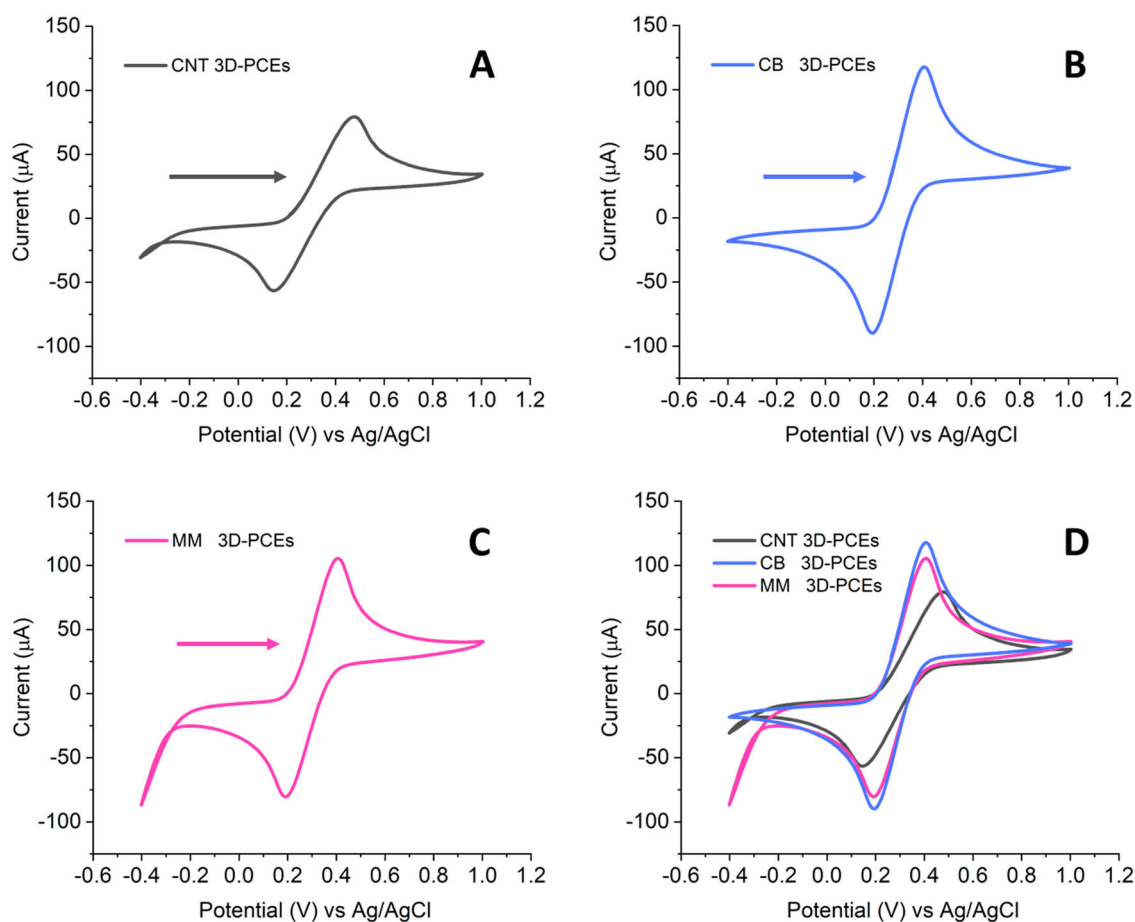
Figure 4. (A–C) Cyclic voltammograms (CVs) of CNT 3D-PCEs (A), CB 3D-PCEs (B), and MM 3D-PCEs (C) and comparison of the CV of the different 3D-PCEs (same colour scheme) (D). $n = 3$ electrodes of each kind were investigated. CVs were recorded in 1.5 mM FcMeOH using a scan rate of 50 mV s^{-1}. The arrow represents the initial scan direction.

3D-PCEs, which have very similar calculated values. In turn, this higher exchange current intensity leads to a smaller charge transfer resistance for the CNT 3D-PCEs compared to the other two.

Contrarily, peak-to-peak separation measurements (ΔE) reveal smaller separations for CB and MM 3D-PCEs compared to the larger separation observed in CNT 3D-PCEs. Furthermore, we calculated the electron transfer rate constant, k^0. The obtained values are supported by the literature data. It was reported that the heterogeneous electron transfer (HET) rates between the electrode surface and a redox marker such as the electrolyte Fe[(CN)$_6$]$^{4-/3-}$ varied depending on the carbon allotrope used to carry out the electrochemical experiments owing to their structure, hybridisation, and surface area [43]. Therefore, 1D CNTs with their nanometre range diameter provide a high surface area to volume ratio, which makes the material ideal for sensing applications. However, the HET of CNTs is slower than that observed for pyrolytic graphite species and amorphous carbon black, which usually show higher carrier mobility

[69–71]. Thus, CNT 3D-PCEs show lower k^0 values than CB 3D-PCEs, as it would be expected. Moreover, the MM 3D-PCEs show faster HET than CNT 3D-PCEs and slower HET than CB 3D-PCEs, showing a closer behaviour to the latter with high HET while only exposing one face of each carbon species. The electroactive area (A) was calculated from CV data using the modified Randles-Sevčik equation (more information in the SI): [72]

$$Ip = (2.69 \times 10^5)n^{3/2}(D \cdot v)^{1/2}A \cdot C$$

In this equation, 'n' is the number of electrons involved in the process (1 electron for the reduction/oxidation of ferrocenemethanol), 'v' is the scan speed, 'C' is the concentration of the electroactive species (1.5 mM), and 'D' the diffusion coefficient (6.3E-6 cm^2 s^{-1}). The calculated electroactive areas from the Ip vs $v^{1/2}$ plot (Figure S4) were in good agreement with the calculated geometrical area for all the electrodes (0.57 cm^2), presenting negative deviations. Such deviations have been observed before and can be related to the

presence of residual superficial PLA filler left after the chemical activation or to the chosen printing parameters, which have been studied, revealing important effects in the calculation of the electroactive area [73]. In short, these results suggest that CB 3D-PCEs allow for the fastest electron transfer rate, followed by MM and CNT 3D-PCEs while showing an opposite tendency for the reversibility of the redox process on their surface [74]. Importantly, one-way ANOVA statistical analysis performed on the different calculated parameters revealed some relevant information. For all the parameters calculated from the recorded current in each of the electrodes (i_0, R_{ct}, and A), the statistical analysis reveals no significant differences between types of electrodes, always giving rise to F values between 0.01 and 0.09. On the other hand, the parameters calculated from data recorded from the potential (ΔE, K^0) showed significant differences between all the electrodes with F values always beyond 5.

All in all, it may seem that the electrochemical data analysis should be complete at this point. Nonetheless, a closer look at the CV plots reveals some unexpected features that might go unnoticed if the data is analyzed just from a mathematical point of view. Thus, the focus should now be on the lower potential region, where the water splitting occurs. On the one hand, when CNT 3D-PCEs (Figure 4(A)) are cycled from −0.3 to −0.4 V a current decrease can be observed, typically associated with the water splitting process due to the inherent impurities of the carbon filament [17]. On the other hand, this current decrease is not observed for CB 3D-PCEs (Figure 4(B)). Curiously, and contrarily to the CB-3DPCEs, in the same region, MM 3D-PCEs show a sharper current decrease to that observed in CNT 3D-PCEs (Figure 4(C)), reaching lower current values and demonstrating a higher activity towards the water splitting. For the sake of comparison, all the CVs have been plotted in Figure 4(D), which shows that while CB 3D-PCEs do not show a current decrease, in the same region there is a current decrease for CNT and MM 3D-PCEs, with the latter affording lower intensity values. This behaviour for the MM 3D-PCEs is unexpected, as the water splitting phenomenon in carbon 3D-printed electrodes, as mentioned above, has been associated with metallic impurities. Thus, the higher activity towards the water splitting could be explained by the increased electroactive area of MM-3DPCEs compared to CNT 3D-PCEs, since CNT 3D-PCEs should inherently expose more impurities to the electrolyte than MM 3D-PCEs (2 pure faces of CNT vs 1 CNT face and 1 CB face with CNTs on top). In this regard, the porous nature of the bottom CNT layer of the MM 3D-PCEs might allow the partial diffusion of the electrolyte into the inner

layers of the electrode (2nd layer being CB-based), therefore allowing the MM 3D-PCEs to reach higher currents and improved electrochemical response. This phenomenon of diffusion of the electrolyte into the inner layers of the MM-3DPCE is confirmed by the asymmetric measurements performed covering one side of the electrode at a time and measuring the CV (Figure S6). The CVs obtained for each side of the electrode do not reveal a big difference between both sides, mostly showing very similar behaviour to that of the CB 3D-PCEs. In this sense, it could be concluded that the role of the CNT side in the MM 3D-PCEs is that of providing metallic impurities, enhancing the activity towards catalytic reactions, while the CB side provides the compact packing of graphitic carbon particles that give rise to a significant increase in the measured currents.

In light of these results, HER by means of LSV was studied on all the electrodes to determine if this improved performance for water splitting showed by MM 3D-PCEs can be observed when the HER is studied.

3.1. Hydrogen evolution reaction

HER is nowadays one of the most investigated electrochemical reactions for energy conversion due to the ongoing energetic crisis and is usually employed as a benchmark to determine the electrocatalytic performance of modified electrodes [75]. The linear sweep voltammetry studies carried out herein reveal (Figure 5) a similar trend to that already observed for the small water splitting observed during the CV measurements of the redox marker. In the low potential region (from
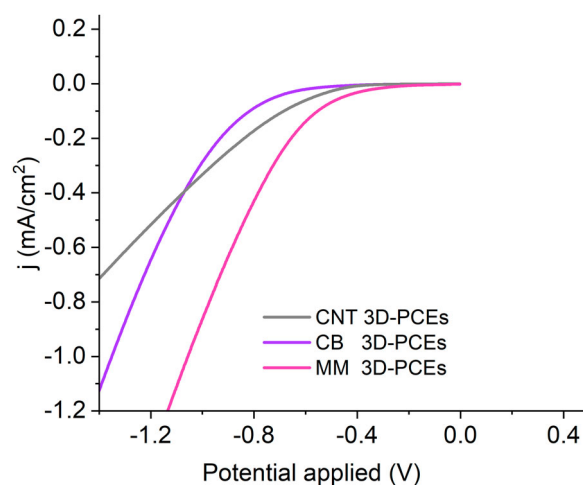

Figure 5. LSV measurements for the HER of MM (pink), CB (purple), and CNT (grey) 3D-PCEs. Conditions: electrolyte, H_2SO_4 (1 M); scan rate, 5mV·s^{-1}. $n = 3$ electrodes of each kind were investigated (the best result is plotted for each type of electrode).
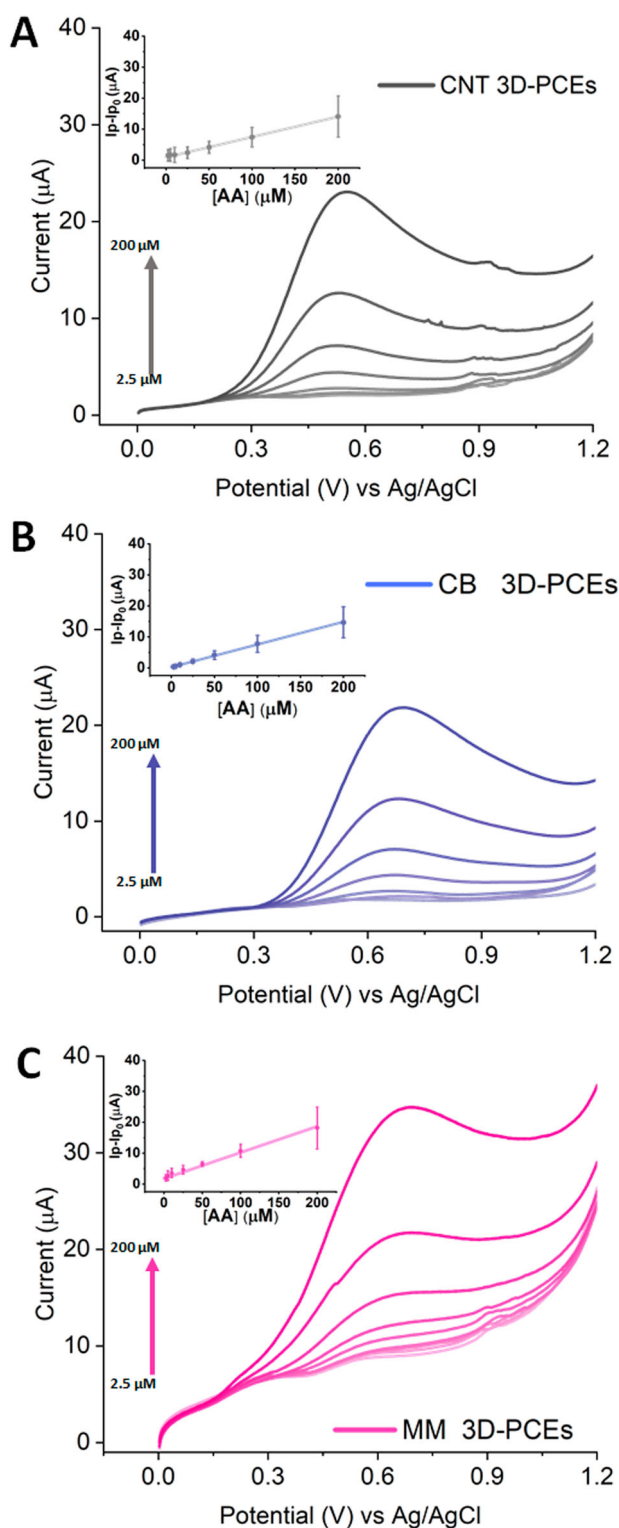
Figure 6. DPV measurements performed for the determination of AA on MM (pink), CB (purple), and CNT (grey) 3D-PCEs. Experiments were carried out in a 0.1 M HNO_3/KNO_3 electrolyte (scan rate: 50 mV·s^{-1}). $n = 3$ electrodes of each kind were investigated.

−0.1 to −0.4 V), CNT and CB 3D-PCEs show linearly decreasing currents with values close to 0 mA, while, in the same region, slightly more negative currents are already recorded for MM 3D-PCEs. Additionally, MM

3D-PCEs are the first electrodes to show a change in slope for the decreasing current at −0.21 V, therefore abandoning the linearity of the current decrease, while CNT and CB 3D-PCEs show their respective change in slope of the recorded current at −0.39 V and −0.51 V. Importantly, although CB 3D-PCEs' current decrease remains linear until lower potentials compared to CNT 3D-PCEs, its slope is much steeper, which leads to the crossing of the currents recorded for both pure material electrodes at −1.07 V in the plot, leading to the final higher activity displayed by CB 3D-PCEs. On the other end, MM 3D-PCEs show a much steeper slope, compared to the other two, demonstrating its higher efficiency for the HER at all times. Translated to overpotential terms, at a current density of −1 mA·cm^{-2}, MM 3D-PCEs display the lowest overpotential of −1.05 V, followed by CB 3D PCEs with −1.35 V and CNT 3D-PCEs, which do not reach those low current density values. In the end, MM 3D-PCEs reach the lowest currents and the lowest over-potential at −1 mA·cm^{-2} of all the 3D-printed materials, followed by CB and CNT 3D-PCEs, which demonstrates the superiority of MM 3D-PCEs towards the HER compared to the pure material electrodes. The origin of this improved performance is associated with two main factors: first, the carbon black-based top side of the MM-3DPCEs leads to a higher active area compared to CNT 3D-PCEs, which translates into higher currents at lower applied potentials; second, the presence of catalytically active metal impurities on the bottom side of MM 3D-PCEs compared to the non-presence of impurities in CB 3D-PCEs enables them towards HER at lower overpotentials. In short, the heterolayered structure of the MM-3DPCEs integrates the best properties of each of their components, giving rise to improved HER efficiency.

To summarise, these results demonstrate an improved performance of the MM 3D-PCEs compared to pristine materials for HER, which was anticipated by the results obtained in the CV measurements of the redox marker. Nonetheless, and even with these interesting results, it should be pointed out that it is hard to foresee the use of these PLA-based electrodes for HER since the conditions employed for this reaction at an industrial scale (NaOH 9 M, 80°C) would inevitably degrade the PLA matrix and deteriorate the electrodes. In light of this outcome, and in order to find a more suitable application for the electrodes, the capability of the MM 3D-PCEs for the detection of ascorbic acid as an analyte in water was also interrogated.

3.2. Ascorbic acid determination

The use of electrochemical techniques for the detection of analytes in water is an appealing strategy since it

allows for a fast, reliable, and cost-effective determination of impurities usually with low limits of detection [8,50,76]. For this purpose, the ability of the different electrodes to detect AA has been explored by performing a calibration experiment by adding different amounts of AA and recording the signal associated with the oxidation of AA (Figure 6(A–C), more information in the experimental section).

For all the electrodes, the addition of successive aliquots of AA results in an increase in the signal recorded for the oxidation of the AA process (Figure 6(A–C)). In terms of potential, CNT 3D-PCEs require the lowest applied potential (0.55 V) for the oxidation of AA, followed by MM and CB 3D-PCEs, which share very similar oxidation potentials (0.69 and 0.70 V). This fact contrasts heavily with the tendency observed during the CV measurements, where CNT 3D-PCEs showed the highest required potential for the oxidation of the redox marker. It should be noted that residual current is recorded for all the electrodes when no AA is added to the media. To avoid an overestimation of the electrode's sensibility, the background signal 'Ip_0' has not been considered by deducting it from the peak current 'Ip' in all cases. In this way, the signals recorded for all the electrodes become comparable (independently of their composition). In general terms, all the calibration curves (Figure 6(A–C) **insets**) can be fitted linearly with the formula $y = a + bx$, where 'a' and 'b' represent the intercept and the slope of the equation, respectively, while 'y' and 'x' refer to the Ip-Ip_0 (in μA) and the final concentration of AA in the solution (in μM), in respective order. All in all, the calculated equations were $y = 0.064x + 1.109$ for CNT 3D-PCEs, $y = 0.072x + 0.309$ for CB 3D-PCEs, and $y = 0.080x + 2.481$ for MM 3D-PCEs. In all cases, the R^2 obtained for the fitting is equal to or above 0.99, which demonstrates the suitability of all the electrodes for the AA determination in the range of concentrations from 2.5 μM to 200 μM. In terms of performance, the best sensibility is displayed by the MM 3D PCEs with a slope of 0.080 ($\pm$0.002) μA μM^{-1}, followed by CB and CNT 3D-PCEs with slopes of 0.072 ($\pm$0.001) μA· μM^{-1} and 0.064 ($\pm$0.001) μA μM^{-1}, respectively. Therefore, the current registered for the MM 3D-PCEs is, at least, 1.1 times higher than that recorded at the same AA concentration for the pure material electrodes, demonstrating its superior capabilities for the sensing of the analyte.

4. Conclusions

Herein, heterolayered 3D-printed carbon electrodes (3D-PCEs) consisting of two alternating commercially available CNT/PLA and CB/PLA conductive nanocomposite filaments were fabricated for the first time (MM 3D-PCEs) via multi-material 3D printing. After their chemical activation, the morphological characterisation revealed the asymmetric surface with the exposed 1D and 3D nanocarbon allotropes. The electrochemical characterisation demonstrates that MM 3D-PCEs' electrochemical properties are between those of the pure material electrodes, although statistical analysis reveals no significant differences between electrodes. Contrarily, when applications such as hydrogen evolution reaction (HER) or detection of ascorbic acid (AA) are the subject of study, MM 3D-PCEs show an improved performance compared to the electrodes purely built with one single allotrope of carbon. The origin of this improvement has been associated with the heterolayered structure of the electrodes, which enables the presence of metallic impurities in MM 3D-PCEs compared to CB 3D-PCEs; and to the higher active area of MM 3D-PCEs compared to CNT 3D-PCEs. Thus, the multi-material printing strategy followed herein, based on alternating layers of different carbon filaments, allows for easy, fast, and scalable preparation of carbon electrodes with improved performance. At the same time, this strategy lays the foundation for the development of a new generation of heterolayered MM-3DPCEs with different electroactive materials such as 2D materials, an appealing strategy for the preparation of heterolayered structures for supercapacitors, batteries, or bio-sensors.

Disclosure statement

No potential conflict of interest was reported by the author(s).

Author contributions

M.P.-C activated the electrodes and recorded SEM images. J.M. and M.S. performed electrochemical measurements. K.G carried out XRD, Raman Spectroscopy and conductivity measurements. S.W. performed electrochemical

measurements and printed the electrodes. M.P.-C and M.P. conceptualised the work. M.P. supervised this work. All authors have contributed to the writing and have given approval to the final version of the manuscript.

References

[1] Chua CK, Leong KF. *3D printing and additive manufacturing: principles and applications: the 5th edition of rapid prototyping: principles and applications*; 2017. 1–426. doi: 10.1142/10200

[2] Tofail SAM, Koumoulos EP, Bandyopadhyay A, et al. Additive manufacturing: scientific and technological challenges, market uptake and opportunities. Mater Today. 2018;21(1):22–37. doi: 10.1016/j.mattod.2017.07.001

[3] Ambrosi A, Pumera M. 3D-Printing technologies for electrochemical applications. Chem Soc Rev. 2016;45(10):2740–2755. doi: 10.1039/C5CS00714C

[4] Shahrubudin N, Lee TC, Ramlan R. An overview on 3D printing technology: technological, materials, and applications. Procedia Manuf. 2019;35:1286–1296. doi: 10.1016/j.promfg.2019.06.089

[5] Stefano JS, Guterres e Silva LR, Rocha RG, et al. New conductive filament ready-to-use for 3D-printing electrochemical (Bio)sensors: towards the detection of SARS-CoV-2. Anal Chim Acta. 2022;1191:339372. doi: 10.1016/j.aca.2021.339372

[6] Muñoz J, Pumera M. 3D-Printed COVID-19 immunosensors with electronic readout. Chem Eng J. 2021;425:131433. doi: 10.1016/j.cej.2021.131433

[7] Redondo E, Pumera M. Fully metallic copper 3D-printed electrodes via sintering for electrocatalytic biosensing. Appl Mater Today. 2021;25:101253. doi: 10.1016/j.apmt.2021.101253

[8] Walters JG, Ahmed S, Terrero Rodríguez IM, et al. Trace analysis of heavy metals (Cd, Pb, Hg) using native and modified 3D printed graphene/poly(lactic acid) composite electrodes (Cd, Pb, Hg) using native and modified 3D printed graphene/poly(lactic acid) composite electrodes. Electroanalysis. 2020;32(4):859–866. doi: 10.1002/elan.201900658

[9] Cardoso RM, Silva PRL, Lima AP, et al. 3D-Printed graphene/polylactic acid electrode for bioanalysis: biosensing of glucose and simultaneous determination of uric acid and nitrite in biological fluids. Sensors Actuators, B Chem. 2020;307:127621. doi: 10.1016/j.snb.2019.127621

[10] Hamzah HH, Keattch O, Yeoman MS, et al. Three-dimensional-printed electrochemical sensor for simultaneous dual monitoring of serotonin overflow and circular muscle contraction. Anal Chem. 2019;91(18):12014–12020. doi: 10.1021/acs.analchem.9b02958

[11] Richter EM, Rocha DP, Cardoso RM, et al. Complete additively manufactured (3D-printed). electrochemical sensing platform. Anal Chem. 2019;91(20):12844–12851. doi: 10.1021/acs.analchem.9b02573

[12] Katic V, Dos Santos PL, Dos Santos MF, et al. 3D printed graphene electrodes modified with prussian blue: emerging electrochemical sensing platform for peroxide detection. ACS Appl Mater Interfaces. 2019;11(38):35068–35078. doi: 10.1021/acsami.9b09305

[13] Manzanares Palenzuela CL, Novotný F, Krupička P, et al. 3D-Printed graphene/polylactic acid electrodes promise high sensitivity in electroanalysis. Anal Chem. 2018;90(9):5753–5757. doi: 10.1021/acs.analchem.8b00083

[14] Jyoti, Redondo E, Alduhaish O, et al. 3D-Printed nanocarbon sensors for the detection of chlorophenols and nitrophenols: towards environmental applications of additive manufacturing. Electrochem Commun. 2021;125:106984. doi: 10.1016/j.elecom.2021.106984

[15] Muñoz J, Redondo E, Pumera M. Versatile design of functional organic–inorganic 3D-printed (Opto) electronic interfaces with custom catalytic activity. 2021;17(41):2103189. doi: 10.1002/smll.202103189

[16] Urbanová V, Plutnar J, Pumera M. Atomic layer deposition of electrocatalytic layer of MoS2 onto metal-based 3D-printed electrode toward tailoring hydrogen evolution efficiency. Appl Mater Today. 2021;24:101131. doi: 10.1016/j.apmt.2021.101131

[17] Browne MP, Urbanova V, Plutnar J, et al. Inherent impurities in 3D-printed electrodes are responsible for catalysis towards water splitting. J Mater Chem A. 2020;8(3):1120–1126. doi: 10.1039/C9TA11949C

[18] Hughes JP, Dos Santos PL, Down MP, et al. Single step additive manufacturing (3D printing) of electrocatalytic anodes and cathodes for efficient water splitting. Sustain Energy Fuels. 2020;4(1):302–311. doi: 10.1039/C9SE00679F

[19] Iffelsberger C, Ng S, Pumera M. Catalyst coating of 3D printed structures via electrochemical deposition: case of the transition metal chalcogenide MoSx for hydrogen evolution reaction. Appl Mater Today. 2020;20:100654. doi: 10.1016/j.apmt.2020.100654

[20] Parra-Cabrera C, Achille C, Kuhn S, et al. 3D printing in chemical engineering and catalytic technology: structured catalysts, mixers and reactors. Chem Soc Rev. 2018;47(1):209–230. doi: 10.1039/C7CS00631D

[21] Frederickson LD, Hausen DM. Infrared spectra-structure correlation study of vanadium-oxygen compounds. Anal Chem. 1963;35(7):818–827. doi: 10.1021/ac60200a018

[22] Ng S, Iffelsberger C, Michalička J, et al. Atomic layer deposition of electrocatalytic insulator Al2O3on three-dimensional printed nanocarbons. ACS Nano. 2021;15(1):686–697. doi: 10.1021/acsnano.0c06961

[23] Wang X, Chen XZ, Alcântara CCJ, et al. MOFBOTS: metal–organic-framework-based biomedical microrobots. Adv Mater. 2019;31(27):1901592. doi: 10.1002/adma.201901592

[24] Terzopoulou A, Wang X, Chen XZ, et al. Biodegradable metal–organic framework-based microrobots (MOFBOTs). Adv Healthc Mater. 2020;9(20):2001031. doi: 10.1002/adhm.202001031

[25] Browne MP, Redondo E, Pumera M. 3D printing for electrochemical energy applications. Chem Rev. 2020;120(5):2783–2810. doi: 10.1021/acs.chemrev.9b00783

[26] Muñoz J, Redondo E, Pumera M. Bistable (supra)molecular switches on 3D-printed responsive interfaces with electrical readout. ACS Appl Mater Interfaces. 2021;13(11):12649–12655. doi: 10.1021/acsami.0c14487

[27] Muñoz J, Palacios-Corella M, Pumera M. Electrically Reading a light-driven molecular switch on 2D-Ti3C2Tx MXene via molecular engineering: towards responsive MXetronics. J Mater Chem A. 2022;10(32):17001–17008. doi: 10.1039/D2TA03349F

[28] Acun A, Zhang L, Bampoulis P, et al. Germanene: the germanium analogue of graphene. J Phys Condens Matter. 2015;27(44):443002. doi: 10.1088/0953-8984/27/44/443002

[29] Maurel A, Courty M, Fleutot B, et al. Highly loaded graphite-polylactic acid composite-based filaments for lithium-Ion battery three-dimensional printing. Chem Mater. 2018;30(21):7484–7493. doi: 10.1021/acs.chemmater.8b02062

[30] Gao W, Pumera M. 3D printed nanocarbon frameworks for Li-Ion battery cathodes. Adv Funct Mater. 2021;31(11):2007285. doi: 10.1002/adfm.202007285

[31] Gao W, Michalička J, Pumera M. Hierarchical atomic layer deposited V2O5 on 3D printed nanocarbon electrodes for high-performance aqueous zinc-ion batteries. 2022;18(1):e2105572. doi: 10.1002/smll.202105572

[32] Palacios-Corella M, Ghosh K, Redondo E, et al. Polyoxometalate-enhanced 3D-printed supercapacitors. ChemSusChem. 2022;15(23):e202201490. doi: 10.1002/cssc.202201490

[33] Omar MH, Razak KA, Ab Wahab MN, et al. Recent progress of conductive 3D-printed electrodes based upon polymers/carbon nanomaterials using a fused deposition modelling (FDM) method as emerging electrochemical sensing devices. RSC Adv. 2021;11(27):16557–16571. doi: 10.1039/D1RA01987B

[34] Honeychurch KC, Rymansaib Z, Iravani P. Anodic stripping voltammetric determination of zinc at a 3-D printed carbon nanofiber–graphite–polystyrene electrode using a carbon pseudo-reference electrode. Sensors Actuators, B Chem. 2018;267:476–482. doi: 10.1016/j.snb.2018.04.054

[35] Iffelsberger C, Jellett CW, Pumera M. 3D printing temperature tailors electrical and electrochemical properties through changing inner distribution of graphite/polymer. 2021;17(24):2101233. doi: 10.1002/smll.202101233

[36] Gonzalez G, Chiappone A, Roppolo I, et al. Development of 3D printable formulations containing CNT with enhanced electrical properties. Polymer (Guildf). 2017;109:246–253. doi: 10.1016/j.polymer.2016.12.051

[37] Vernardou D, Vasilopoulos KC, Kenanakis G. 3D printed graphene-based electrodes with high electrochemical performance. Appl Phys A Mater Sci Process. 2017;123(10):doi: 10.1007/s00339-017-1238-1

[38] Vaněčková E, Bouša M, Nováková Lachmanová Š, et al. 3D printed polylactic acid/carbon black electrodes with nearly ideal electrochemical behaviour. J Electroanal Chem. 2020;857:113745. doi: 10.1016/j.jelechem.2019.113745

[39] Kalinke C, de Oliveira PR, Neumsteir NV, et al. Influence of filament aging and conductive additive in 3D printed sensors. Anal Chim Acta. 2022;1191:339228. doi: 10.1016/j.aca.2021.339228

[40] Vaněčková E, Bouša M, Nováková Lachmanová Š, et al. 3D printed polylactic acid/carbon black electrodes with nearly ideal electrochemical behaviour. J Electroanal Chem. 2020;857:113745. doi: 10.1016/j.jelechem.2019.113745

[41] Kalinke C, Neumsteir NV, Aparecido GDO, et al. Comparison of activation processes for 3D printed PLA-graphene electrodes: electrochemical properties and application for sensing of dopamine. Analyst. 2020;145(4):1207–1218. doi: 10.1039/C9AN01926J

[42] Laurila T, Sainio S, Caro M. Hybrid carbon based nanomaterials for electrochemical detection of biomolecules. Prog Mater Sci. 2017;88:499–594. doi: 10.1016/j.pmatsci.2017.04.012

[43] Villarreal CC, Pham T, Ramnani P, et al. Carbon allotropes as sensors for environmental monitoring. Curr Opin Electrochem. 2017;3(1):106–113. doi: 10.1016/j.coelec.2017.07.004

[44] Baptista FR, Belhout SA, Giordani S, et al. Recent developments in carbon nanomaterial sensors. Chem Soc Rev. 2015;44(13):4433–4453. doi: 10.1039/C4CS00379A

[45] Lopes JMJ, Vignaud D. Molecular beam epitaxy. Mol Beam Ep. 2018: 487–513. doi: 10.1016/B978-0-12-812136-8.00023-2

[46] Jiang JW, Park HS. Mechanical properties of MoS2/graphene heterostructures. Appl Phys Lett. 2014;105(3):033108. doi: 10.1063/1.4891342

[47] Wythers MC. Advances in materials science research. Adv Mater Sci Res. 2011;3:1–338.

[48] Rocha DP, Albuquerque RBA, Oliveira GP, et al. Encyclopedia of sensors and biosensors. Encycl Sensors Biosens. 2023: 73–88. doi: 10.1016/B978-0-12-822548-6.00021-2

[49] Laurila T, Sainio S, Caro M. Hybrid carbon based nanomaterials for electrochemical detection of biomolecules. Prog Mater Sci. 2017;88:499–594. doi: 10.1016/j.pmatsci.2017.04.012

[50] Contreras-Naranjo JE, Perez-Gonzalez VH, Mata-Gómez MA, et al. 3D-printed hybrid-carbon-based electrodes for electroanalytical sensing applications. Electrochem Commun. 2021;130:107098. doi: 10.1016/j.elecom.2021.107098

[51] Li F, Macdonald NP, Guijt RM, et al. Increasing the functionalities of 3D printed microchemical devices by single material, multimaterial, and print-pause-print 3D printing. Lab Chip. 2019;19(1):35–49. doi: 10.1039/C8LC00826D

[52] Guo Y, Liu P, Jiang P, et al. A flow-rate-controlled double-nozzles approach for electrochemical additive manufacturing. Virtual Phys Prototyp. 2022;17(1):52–68. doi: 10.1080/17452759.2021.1989751

[53] Zheng H, Lu X, Jiang P, et al. Numerical simulation of 3D double-nozzles printing by considering a stabilized localized radial basis function collocation method. Addit Manuf. 2022;58:103040. doi: 10.1016/J.ADDMA.2022.103040

[54] Gusmão R, Browne MP, Sofer Z, et al. The capacitance and electron transfer of 3D-printed graphene electrodes are dramatically influenced by the type of solvent used for pre-treatment. Electrochem Commun. 2019;102:83–88. doi: 10.1016/j.elecom.2019.04.004

[55] Browne MP, Novotný F, Sofer Z, et al. 3D printed graphene electrodes' electrochemical activation. ACS Appl Mater Interfaces. 2018;10(46):40294–40301. doi: 10.1021/acsami.8b14701

[56] Redondo E, Ng S, Muñoz J, et al. Tailoring capacitance of 3D-printed graphene electrodes by carbonisation temperature. Nanoscale. 2020;12(38):19673–19680. doi: 10.1039/D0NR04864J

[57] Amorim PHO, Oliveira FQ, dos Santos HC, et al. Smart innovation, systems and technologies. Smart Innov Syst

Technol. 2022;255:249–258. doi: 10.1007/978-981-16-4884-7_20

[58] Rocha Á, Paredes-Calderón M, Guarda T. Developments and advances in defense and security. Proc MICRADS 2020 Conf Proc. 2020;181:556. doi: 10.1007/978-981-16-4884-7

[59] da Silva FD, Rocha RG, Rocha DP, et al. In situ electrochemical exfoliation of embedded graphite to superficial graphene sheets for electroanalytical purposes. Electrochim Acta. 2020;354:136762. doi: 10.1016/j.electacta.2020.136762

[60] Muñoz J, Redondo E, Pumera M. Chiral 3D-printed bioelectrodes. Adv Funct Mater. 2021;31(16):2010608. doi: 10.1002/adfm.202010608

[61] Ghosh K, Ng S, Iffelsberger C, et al. Inherent impurities in graphene/polylactic acid filament strongly influence on the capacitive performance of 3D-printed electrode. Chem - A Eur J. 2020;26(67):15746–15753. doi: 10.1002/chem.202004250

[62] Saito R, Hofmann M, Dresselhaus G, et al. Raman spectroscopy of graphene and carbon nanotubes. Adv Phys. 2011;60(3):413–550. doi: 10.1080/00018732.2011.582251

[63] Foo CY, Lim HN, Mahdi MA, et al. Three-dimensional printed electrode and Its novel applications in electronic devices. Sci Reports. 2018;8(1):1–11. doi: 10.1038/s41598-018-25861-3

[64] Nanaki S, Barmpalexis P, Iatrou A, et al. Risperidone controlled release microspheres based on poly(lactic acid)-poly(propylene adipate) novel polymer blends appropriate for long acting injectable formulations. Pharmaceutics. 2018;10(3):130. doi: 10.3390/pharmaceutics10030130

[65] Singh DK, Iyer PK, Giri PK. Diameter dependence of interwall separation and strain in multiwalled carbon nanotubes probed by x-ray diffraction and Raman scattering studies. Diam Relat Mater. 2010;19(10):1281–1288. doi: 10.1016/j.diamond.2010.06.003

[66] Maniwa Y, Fujiwara R, Kira H, et al. Multiwalled carbon nanotubes grown in hydrogen atmosphere: an x-ray diffraction study. Phys Rev B. 2001;64(7):073105. doi: 10.1103/PhysRevB.64.073105

[67] Glowacki MJ, Cieslik M, Sawczak M, et al. Helium-assisted, helium-assisted, solvent-free electro-activation of 3D printed conductive carbon-polylactide electrodes by pulsed laser ablation. Appl Surf Sci. 2021;556:149788. doi: 10.1016/j.apsusc.2021.149788

[68] dos Santos PL, Katic V, Loureiro HC, et al. Enhanced performance of 3D printed graphene electrodes after electrochemical Pre-treatment: role of exposed graphene sheets. Sensors Actuators B Chem. 2019;281:837–848. doi: 10.1016/j.snb.2018.11.013

[69] Arduini F, Di Giorgio F, Amine A, et al. Electroanalytical characterization of carbon black nanomaterial paste electrode: development of highly sensitive tyrosinase biosensor for catechol detection. Anal Lett. 2010;43(10–11):1688–1702. doi: 10.1080/00032711003653932

[70] Silveri F, Della Pelle F, Scroccarello A, et al. Carbon black functionalized with naturally occurring compounds in water phase for electrochemical sensing of antioxidant compounds. Antioxidants. 2022;11(10):2008. doi: 10.3390/antiox11102008

[71] Deroco PB, Lourencao BC, Fatibello-Filho O. The use of modified electrode with carbon black as sensor to the electrochemical studies and voltammetric determination of pesticide mesotrione. Microchem J. 2017;133:188–194. doi: 10.1016/j.microc.2017.03.024

[72] Laoire CO, Mukerjee S, Abraham KM, et al. Elucidating the mechanism of oxygen reduction for lithium-air battery applications. J Phys Chem C. 2009;113(46):20127–20134. doi: 10.1021/jp908090s

[73] Barbosa JR, Amorim PHO, Mariana MC, et al. Smart innovation, systems and technologies. Smart Innov Syst Technol. 2020;152:425–435. doi: 10.1007/978-981-13-9155-2_34

[74] Heinze J. Cyclic voltammetry—"electrochemical spectroscopy". New analytical methods (25). Chemie Int Ed English. 1984;23(11):831–847. doi: 10.1002/anie.198408313

[75] Akshay Kumar KP, Ghosh K, Alduhaish O, et al. Dip-coating of MXene and transition metal dichalcogenides on 3D-printed nanocarbon electrodes for the hydrogen evolution reaction. Electrochem Commun. 2021;122:106890. doi: 10.1016/j.elecom.2020.106890

[76] Kumar KPA, Ghosh K, Alduhaish O, et al. Metal-plated 3D-printed electrode for electrochemical detection of carbohydrates. Electrochem Commun. 2020;120:106827. doi: 10.1016/j.elecom.2020.106827